

## Investigation into electron cloud effects in the International Linear Collider positron damping ring

J. A. Crittenden,<sup>\*</sup> J. Conway, G. F. Dugan, M. A. Palmer,<sup>†</sup> D. L. Rubin,  
J. Shanks and K. G. Sonnad

*CLASSE, Cornell University, Ithaca, New York 14853, USA*

L. Boon and K. Harkay  
*ANL, Argonne, Illinois 60439, USA*

T. Ishibashi  
*KEK, 1-1 Oho, Tsukuba, Ibaraki 305-0801, Japan*

M. A. Furman  
*LBNL, Berkeley, California 94720, USA*

S. Guiducci  
*INFN Laboratori Nazionali di Frascati, P.O. Box 13, I-00044, Frascati (Rome), Italy*

M. T. F. Pivi<sup>‡</sup> and L. Wang  
*SLAC, Menlo Park, California 94025, USA*  
(Received 13 November 2013; published 17 March 2014)

We report modeling results for electron cloud buildup and instability in the International Linear Collider positron damping ring. Updated optics, wiggler magnets, and vacuum chamber designs have recently been developed for the 5 GeV, 3.2-km racetrack layout. An analysis of the synchrotron radiation profile around the ring has been performed, including the effects of diffuse and specular photon scattering on the interior surfaces of the vacuum chamber. The results provide input to the cloud buildup simulations for the various magnetic field regions of the ring. The modeled cloud densities thus obtained are used in the instability threshold calculations. We conclude that the mitigation techniques employed in this model will suffice to allow operation of the damping ring at the design operational specifications.

DOI: [10.1103/PhysRevSTAB.17.031002](https://doi.org/10.1103/PhysRevSTAB.17.031002)

PACS numbers: 29.20.db, 41.75.Ht, 79.20.Hx, 79.60.Bm

### I. INTRODUCTION

The discoveries at the Large Hadron Collider [1,2] have reintensified interest in the proposed International Linear Collider (ILC) [3]. Operation of the ILC depends critically on the reliable performance of the electron and positron damping rings (DRs) which will serve as injectors. Electron cloud (EC) buildup has been shown to limit the performance of storage rings at KEK-B [4] and PEP-II [5], the operating parameters of which are comparable to those of the ILC DRs. For the past several years, we have been developing and validating modeling

codes for the purpose of designing the ILC DRs. This paper presents the results of those efforts. We present the beam optics design, the vacuum chamber designs including recommended cloud buildup mitigation techniques, cloud buildup simulations and modeling estimates of the effects on beam dynamics, deriving conclusions on the feasibility of building and operating the positron DR to specification.

### II. DESIGN OF THE POSITRON DAMPING RING LATTICE

The lattice design used for the EC buildup and instability simulations is the so-called DTC03 lattice, with arc cells designed by Rubin *et al.* [6] and straights based on the work of Korostelev and Wolski [7]. The lattice has since undergone minor revisions to improve matching between the straights and arc sections, and has iterated to DTC04 [8]. The differences between DTC03 and DTC04 are insignificant for the purposes of the studies described here. The racetrack layout for the 3238-m circumference ring is shown in Fig. 1. The 100-m-long RF straights can accommodate as

<sup>\*</sup>crittenden@cornell.edu

<sup>†</sup>Present address: Fermi National Accelerator Laboratory, P.O. Box 500, Batavia, IL 60510-5011, USA.

<sup>‡</sup>Present address: IMS Nanofabrication, Vienna, Austria.

*Published by the American Physical Society under the terms of the Creative Commons Attribution 3.0 License. Further distribution of this work must maintain attribution to the author(s) and the published article's title, journal citation, and DOI.*

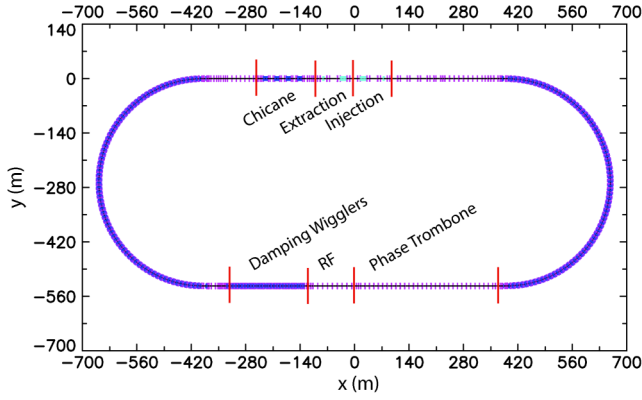


FIG. 1. Layout of DTC04 lattice.

many as 16 single-cell cavities and the 226-m wiggler straight up to 60 superferric wiggler magnets [9].

The operational parameters of the damping ring are given in Table I. The baseline design (26-ms damping time and 5-Hz operation) requires 8 cavities with total accelerating voltage of 14 MV and 54 2.1-m-long wiggler magnets with 1.51-T peak field. In order to run in the proposed 10-Hz mode, the wigglers operate at 2.16 T to cut the radiation damping time in half, and the accelerating voltage is increased to 22.4 MV with 12 cavities to preserve the 6-mm bunch length. The 339-m phase trombone in the wiggler straight consists of five six-quadrupole cells and has a tuning range of  $\pm 0.5$  betatron wavelengths. The opposite straight includes injection and extraction lines, and the 117-m-long chicane for fine adjustment of the revolution period. The range of the chicane is  $\pm 4.5$  m with negligible contribution to the horizontal emittance. The arc cell, shown in Fig. 2, is a simple variation of a TME-style cell with a single 3-m bend, three quadrupoles (one focusing and two defocusing), four sextupoles, a skew quadrupole, and two beam position monitors. Figure 3 shows the beta functions and horizontal dispersion function for the entire DTC04 lattice. There are 75 cells in each arc.

TABLE I. Summary of the DTC04 lattice parameters.

Parameter	Value	Units
Circumference	3238	m
Energy	5.0	GeV
Betatron tunes ( $Q_x, Q_y$ )	(48.850, 26.787)	
Chromaticity ( $\xi_x, \xi_y$ )	(1.000, 0.302)	
Train repetition rate	5	Hz
Minimum bunch spacing	6.15	ns
Bunch population	$2 \times 10^{10}$	
Extracted $\epsilon_x^{\text{geometric}}$	0.6	nm
Extracted $\epsilon_y^{\text{geometric}}$	$< 2$	pm
Extracted bunch length	6	mm
Extracted $\sigma_E/E$	0.11	%
Damping time	24	ms
Wiggler $B^{\text{max}}$	1.5	T

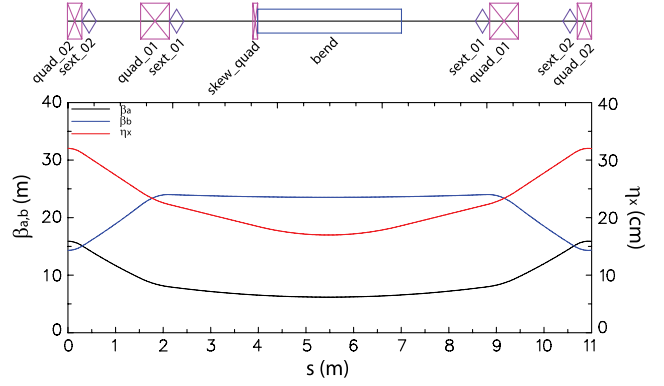


FIG. 2. Horizontal and vertical beta functions  $\beta_a$  and  $\beta_b$ , and the horizontal dispersion function  $\eta_x$  in the DTC04 arc cell.

A complete list of components is given in Table II. The dynamic aperture including magnet multipole errors and misalignments, and wiggler nonlinearities, is large enough to accept an injected positron phase space with normalized horizontal and vertical emittances  $A_x$  and  $A_y$  such that  $A_x + A_y < 0.07$  mrad and energy spread  $\Delta E/E \leq 0.075\%$  [10].

### III. VACUUM CHAMBER DESIGN

The conceptual design of the vacuum chambers incorporates mitigation techniques in each of the various magnetic field environments to suppress the local buildup of the EC. The mitigation methods were selected based on the results of an intense research effort conducted as part of the ILC technical design program [11]. The vacuum system conceptual design is described in Ref. [12]. The vacuum chamber profiles chosen for the wiggler, arc, dipole, and fieldfree regions of the ring are shown in Fig. 4. In the arc regions of the ring, the 50-mm aperture vacuum chambers employ a TiN coating to suppress secondary electron yield (SEY) and dual antechambers to reduce the number of photoelectrons which can seed the cloud. The rear walls of the antechambers are angled in order to suppress photon backscattering into the beam region. In the dipoles, the EC is further suppressed by the use of longitudinal grooves on the top and bottom surfaces, as shown in Figs. 4(c) and 5. In the wiggler region, a 46-mm aperture chamber utilizes clearing electrodes (see Figs. 6 and 7) to suppress growth of the cloud and dual antechambers along with custom photon stops to suppress the generation of photoelectrons. Drift regions throughout the ring will employ solenoid windings to further reduce the EC density in the vicinity of the beam.

### IV. PHOTON TRANSPORT MODEL

The distribution of synchrotron radiation striking the walls of the vacuum chamber can be used to predict the sources of the photoelectrons which seed the EC. This distribution has been computed for the ILC DR lattice using a newly developed photon-tracking simulation code,

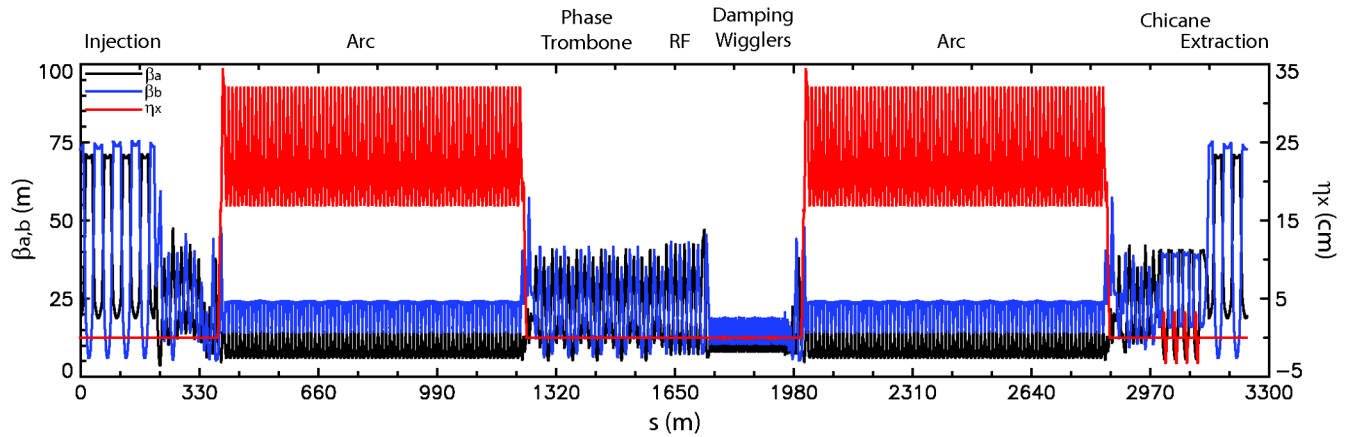


FIG. 3. Horizontal and vertical beta functions  $\beta_a$  and  $\beta_b$ , and the horizontal dispersion function  $\eta_x$  for the entire DTC04 lattice.

SYNRAD3D [13]. This code computes the synchrotron radiation photons per positron generated by a beam circulating in the magnetic lattice, and simulates the propagation in three dimensions of the photons as they scatter off, or are absorbed by, the vacuum chamber. The design vacuum chamber geometry, including details such as antechambers and photon stops, is used in the calculation. Both specular and diffuse photon scattering are included in the simulation. For the scattering calculation, the surface material is approximated as aluminum with a thin carbon coating, and the surface roughness parameters are typical of a technical vacuum chamber, namely rms roughness  $0.1 \mu\text{m}$  and autocorrelation length  $5 \mu\text{m}$ .

Figure 8 shows the photon intensity distributions for magnetic elements in one of the arcs of the DR. The low photon rates at zero and  $\pi$  radians are due to the antechambers. The top-bottom asymmetry is due to the angle in the antechamber back walls, which inhibits scattering out of the antechamber.

This photon transport model was also used to calculate the consequences of photon scattering for the vacuum chamber heat load. In particular, the synchrotron radiation produced by the superconducting wiggler magnets produces intense heating on the vacuum chamber walls. Photon absorbers are used to shield the central region of the beam chamber in the superconducting wigglers [14].

Each wiggler magnet produces 25.2 kW of synchrotron radiation power. Since the wiggler straight is 200 m long most of this power will be absorbed within the wiggler section. The photon absorbers were designed to absorb 40 kW of radiation power each [15]. The modeled 499 mm-long conical absorbers have diameters varying from 44 mm to 52 mm and are placed between pairs of damping wiggler magnets. The synchrotron radiation is incident on a 23-mm long tapered section at the end of the absorber.

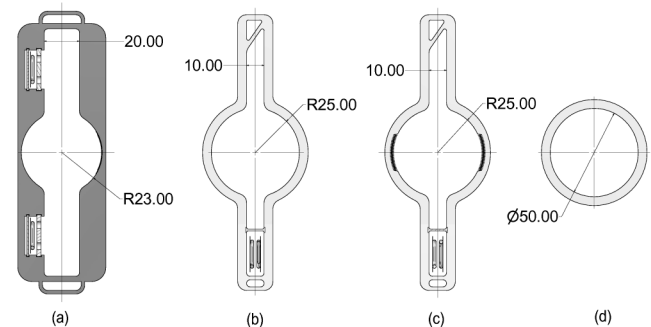


FIG. 4. Vacuum chamber profiles for the (a) wiggler magnets, (b) arc sections, (c) dipole magnets, and (d) fieldfree regions of the damping ring. Note the positions of the NEG strips, the grooves in the dipole vacuum chambers and the angled rear walls of the antechambers.

TABLE II. Summary of elements in the DTC04 lattice.

Class	Count
Beam position monitor	511
Dipole	164
Horizontal steering	150
Vertical steering	150
Combined H+V steering	263
Quadrupole	813
Skew quadrupole	160
Sextupole	600
Damping wigglers	54

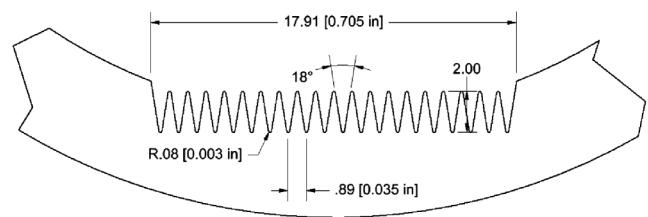


FIG. 5. Schematic cross section of bottom wall showing the dimensions of the grooves used to suppress EC buildup in the dipole magnets.

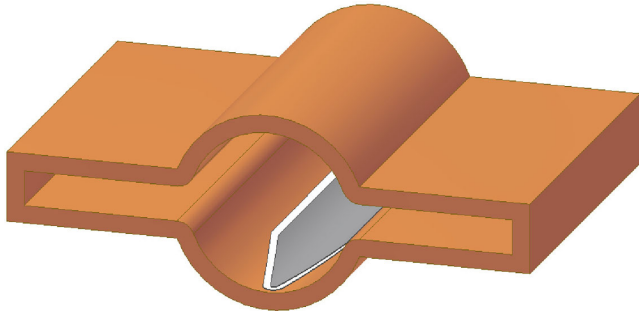


FIG. 6. Wiggler magnet vacuum chamber showing the clearing electrode.

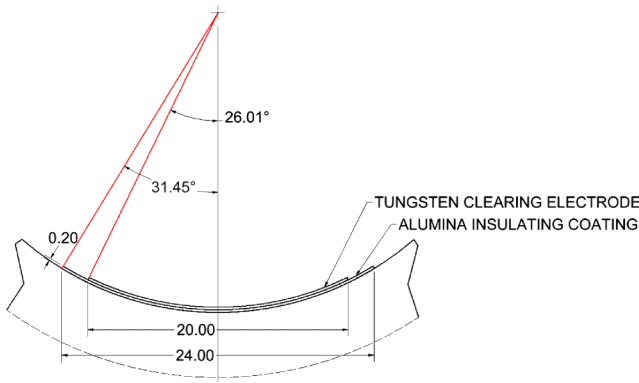


FIG. 7. Dimensions of the clearing electrode designed for cloud suppression in the wiggler magnets.

The method described in [16] was used to calculate the total power dissipated in each photon absorber. We compared the dissipated power for three models of photon scattering: no scattering, specular scattering, and diffuse scattering. The first case assumed that all photons incident on the chamber wall are absorbed, yielding maximum absorbed power of 40.3 kW. This result agrees with previous analytical calculations presented in Ref. [15] for the 6.4 km damping ring. The specular scattering model used a reflectivity based on a surface roughness of 4 nm rms, yielding a maximum power of 42.9 kW. The model for diffuse scattering assumed the surface roughness parameters typical of a technical aluminum vacuum chamber, 0.1  $\mu\text{m}$  rms and 5  $\mu\text{m}$  autocorrelation length, resulting in maximum power of 41.0 kW. The calculated absorbed power for this model and an exponential fit are shown in Fig. 9. We conclude that the absorber design is capable of handling the synchrotron radiation power produced by the damping wigglers.

### V. EC BUILDUP IN THE ARC DIPOLES

We have employed the code POSINST [17], to simulate EC buildup in the arc dipoles of the ILC DR lattice [18] under the following assumptions: (i) the SEY model

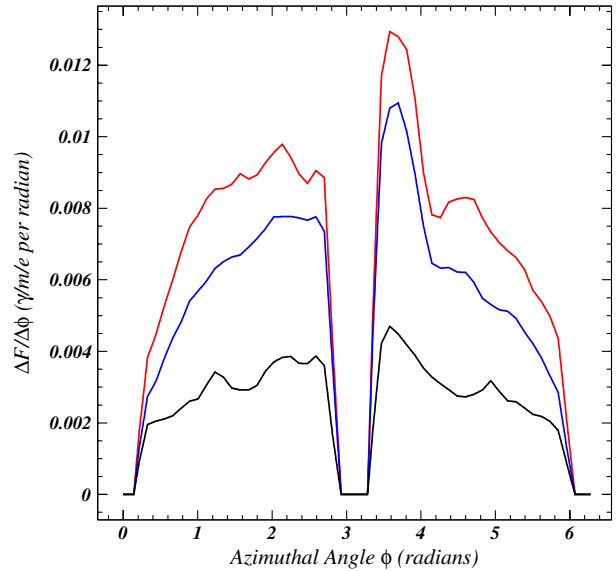


FIG. 8. Absorbed photon rate per radian  $\frac{\Delta F}{\Delta\phi}(\phi)$  versus azimuthal angle  $\phi$  in Arc 1 of the DR, averaged over the regions corresponding to three types of magnetic environment: (i) quadrupole fields (red), (ii) fieldfree regions (blue), and (iii) dipole fields (black). The azimuthal angle  $\phi$  is defined to be zero where the vacuum chamber intersects the bend plane on the outside of the ring. The angle  $\pi/2$  corresponds to the top of the vacuum chamber. The low photon rates at zero and  $\pi$  radians are due to the absorption in the antechambers.

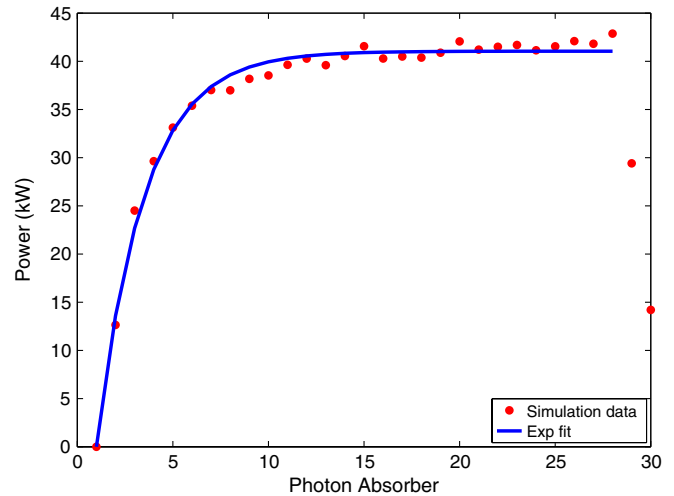


FIG. 9. Exponential fit to the calculated power dissipated on each photon absorber in the damping wiggler straight section.

parameters are those obtained from fits to measurements obtained at the Cornell Electron Storage Ring Test Accelerator (CESRTA) project [19] for a TiN surface [20], (ii) the distribution of photons striking the chamber surface at the location of the dipole magnet has been obtained from SYNRAD3D calculations including photon scattering, and (iii) the quantum efficiency is assumed to be 0.05, independent of photon energy and incident angle.

TABLE III. POSINST modeling results for EC densities  $N_e$  ( $10^{11} \text{ m}^{-3}$ ) in the dipole regions of the ILC DR lattice. The first row shows the beam-pipe-averaged density at the end of a 34-bunch train. The second row shows the peak  $20\sigma$  density during the train passage. The third row gives the maximum  $20\sigma$  density just prior to the arrival of any bunch.

SEY	0	0.94
34-bunch density	0.5	1.2
Peak $20\sigma$ density	0.2	0.5
$20\sigma$ density prior to bunch arrival	0.2	0.4

The SEY model corresponding to the above-mentioned fits yields a peak SEY value of 0.94 at an incident electron energy of 296 eV. In addition, we have carried out the simulation in which the SEY is set to 0 (meaning that any electron hitting the chamber walls gets absorbed with unit probability) in order to isolate the contribution to the EC density  $N_e$  from photoemission. The results are summarized in Table III. Cloud densities averaged over the full vacuum chamber in the 1-m-long test volume as well as those averaged over a  $20\sigma_x \times 20\sigma_y$  elliptical cross-sectional area centered on the beam axis, where  $\sigma_x$  and  $\sigma_y$  denote the horizontal and vertical rms beam sizes, are shown. The modeling statistical uncertainties are less than 30%.

The results of the simulation with no secondary electron production provide a lower limit on  $N_e$ ; however, one must bear in mind that this lower limit is directly proportional to the model value for the quantum efficiency, here assumed to be 5%. For peak SEY = 0.94,  $N_e$  is a factor of 2 or 3 greater than that for SEY = 0. These results for peak SEY = 0.94 represent an upper limit, since the effects of the grooves in the dipole vacuum chamber design were not accounted for in the simulation. The  $20\sigma$  densities are somewhat smaller than the above-quoted average over the entire vacuum chamber, as are the  $20\sigma$ -densities prior to bunch passage.

The effectiveness of grooves for suppression of EC buildup has been the subject of a number of modeling studies [21,22]. Measurements of the reduction in secondary yield afforded by such grooves have been performed at PEP-II [23,24]. More recently, measurements of the reduction of cloud buildup in a grooved aluminum vacuum chamber relative to that for a smooth chamber surface in the CESR positron storage ring showed an improvement by more than a factor of two, corresponding to a decrease in the peak SEY value from 2.0 to 1.2 [25].

## VI. EC BUILDUP IN THE QUADRUPOLES, SEXTUPOLES, AND FIELDFREE REGIONS

The EC buildup modeling code ELOUD [26,27] served to calculate estimates of the cloud densities in the quadrupoles and sextupoles in the arc and wiggler regions and in the fieldfree regions of the wiggler sections for the ILC DR

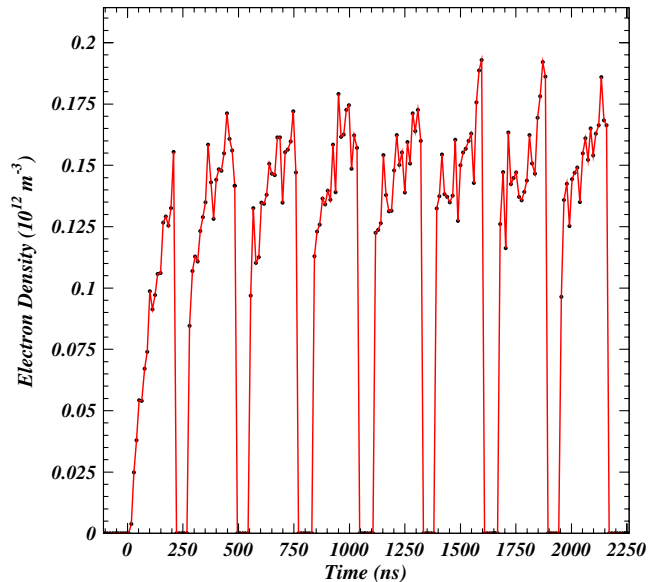


FIG. 10.  $20\sigma$  cloud densities on a beam axis just prior to the passage of each of the 34 bunches in 8 trains in a quadrupole magnet in an arc region of the ILC DR. Cloud trapping effects build up over many train passages, but the maximum central density along a train stabilizes at a value less than  $2 \times 10^{11} \text{ m}^{-3}$  after two trains.

lattice. The photon transport modeling code SYNRAD3D provided photon absorption distributions averaged over each of these regions. The ELOUD code was updated to use the POSINST-style photoelectron production and SEY model parameters [28]. Comparative studies of the ELOUD and

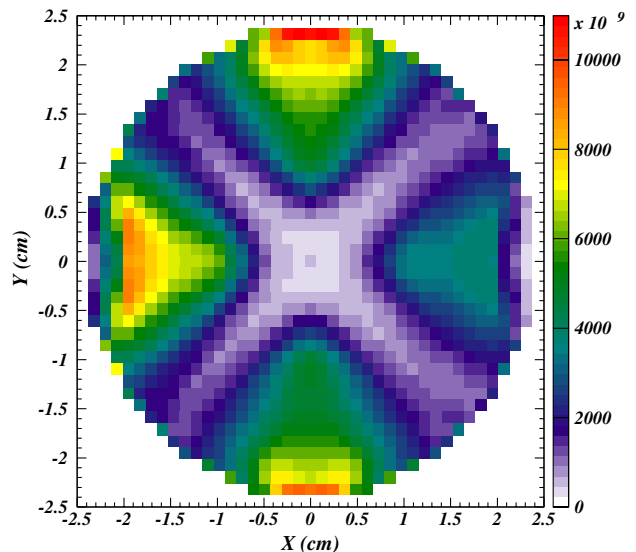


FIG. 11. Simulated EC density profile on a  $41 \times 41$  grid in a quadrupole magnet in an arc region of the ILC CR averaged over the  $2.2 \mu\text{s}$  simulation time. Cloud electron escape zones are observed along the diagonal regions connecting magnet poles, as are several regions of trapped cloud.

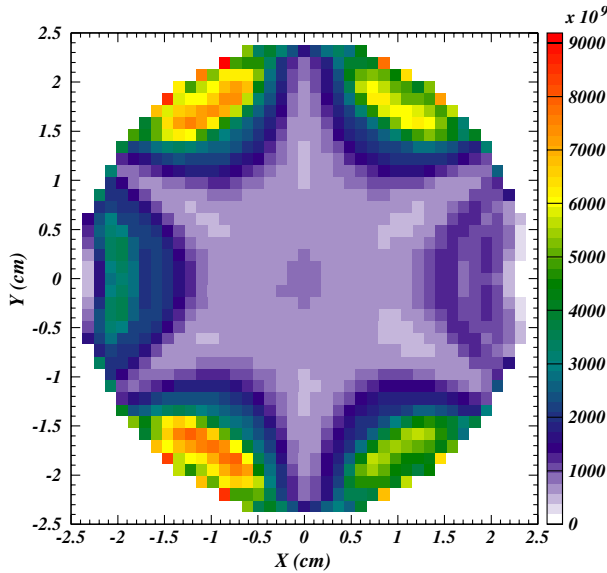


FIG. 12. Simulated EC density profile averaged over the 2.2  $\mu$ s simulation time in an ILC DR sextupole magnet.

POSINST codes, including validation with CESRTA coherent tune shift measurements in dipole magnets have been presented in Refs. [29] and [30]. The ECLLOUD code was also extended to sextupole magnetic fields for the purposes of this study. Representative field strengths of 10 T/m (70 T/m<sup>2</sup>) were used for the quadrupoles (sextupoles). Trapping effects were evident in the beam-pipe-averaged cloud densities, which had not yet reached equilibrium after eight train passages, but since the trapping does not occur in the central beam region, the cloud density in the 20 $\sigma$  beam region just prior to the passage of each bunch (shown in Fig. 10) was stable after just a couple of train passages. Figure 11 shows the cloud density profile averaged over the 2.2  $\mu$ s simulation. The higher density regions, including those with long-term trapped cloud, do not populate the beam axis. The 20 $\sigma$  cloud densities calculated in the field of a sextupole magnet also reach saturation during the first two trains, and the density profile is also depleted on the beam axis, as shown in Fig. 12.

Table IV shows the 20 $\sigma$  density estimates prior to each bunch passage obtained assuming a peak SEY value of

TABLE IV. POSINST and ECLLOUD modeling results for the 20 $\sigma$  density estimates  $N_e$  ( $10^{11} \text{ m}^{-3}$ ) just prior to each bunch passage in the ILC DR lattice design. The total length of each magnetic field environment  $L$  is given in meters.

	Fieldfree		Dipole		Quadrupole		Sextupole	
	L	$N_e$	L	$N_e$	L	$N_e$	L	$N_e$
Arc region 1	406	2.5	229	0.4	146	1.5	90	1.4
Arc region 2	365	2.5	225	0.4	143	1.7	90	1.3
Wiggler region	91	40	0		18	12	0	

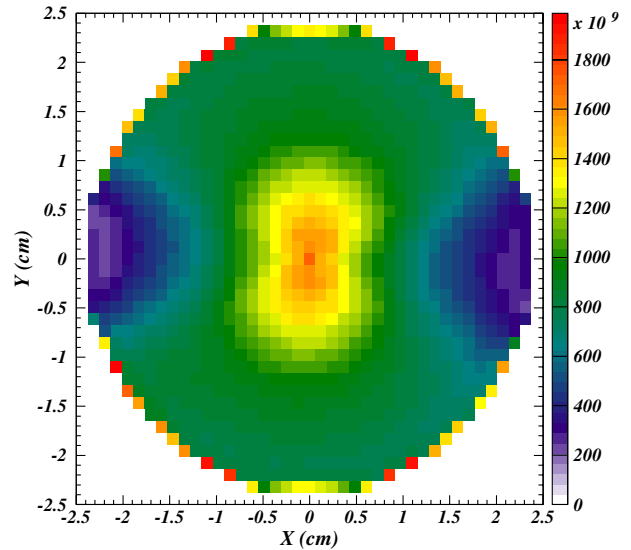


FIG. 13. Simulated EC density profile averaged over the 4.5  $\mu$ s simulation time in a fieldfree region of arc region 1 without application of the solenoidal magnetic field mitigation technique.

0.94. The POSINST results for the arc dipoles are included in this table. The integrated ring lengths for the magnetic environment types are also shown. The high density values in the quadrupole magnets of the wiggler section of the ring result from the intense wiggler radiation. The densities are an order of magnitude greater than those in the arc regions, but the integrated length of those quadrupoles is an order of magnitude smaller. The simulations for the fieldfree regions were repeated imposing a solenoidal magnetic field of 40 G, as is foreseen in the mitigation recommendations determined during the ECLLOUD10 workshop [11]. Such a field was shown to reduce the cloud buildup in the vicinity

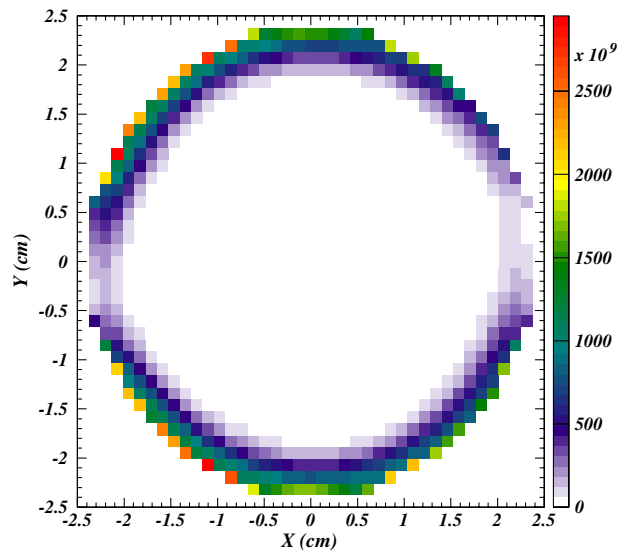


FIG. 14. Effect of a 40-G solenoidal magnetic field on the simulated EC density profile in a fieldfree region of the ring.

of the beam to negligible levels. The  $20\sigma$  cloud density at a time immediately prior to the passage of each of the bunches was found to be  $2.5 \times 10^{11}$  with no applied solenoidal field. Figure 13 shows the cloud profile averaged over the  $4.5 \mu\text{s}$  corresponding to the passage of 16 trains of 34 bunches each. The effect on the cloud profile of a 40-G solenoidal field is shown in Fig. 14.

### VII. EC BUILDUP IN THE WIGGLER MAGNETS

The EC buildup in the wiggler magnets has been simulated using the CLOUDLAND code [31]. The ring length occupied by wigglers is 118 m in the ILC DR lattice design. The simulation assumes a peak SEY of 1.2 at an incident electron energy of 250 eV for the copper surface of the wiggler vacuum chamber. The absorbed photon rate assumed in the simulation is 0.198 photons/m/positron and the azimuthal distribution around the perimeter of the vacuum chamber cross section is approximated as uniform. A quantum efficiency of 10% and rms beam sizes  $\sigma_x/\sigma_y = 80 \mu\text{m}/5.5 \mu\text{m}$  is assumed. The peak wiggler field is 2.1 T. The beam chamber of the wiggler section includes an antechamber with 2.0 cm vertical aperture. Our assumption of a round chamber of inner diameter 46 mm is a reasonable approximation since most electrons accumulate near the vertical midplane due to multipacting. The CLOUDLAND calculation shows that a beam with bunch population of  $2 \times 10^{10}$  and bunch spacing of 6 ns can excite strong multiplication near the vertical midplane. The calculation was performed for a train of 34 bunches followed by a gap of 45 rf buckets.

Figure 15 shows the distribution of the simulated EC in the transverse plane at the longitudinal center of a wiggler pole for the case of no voltage applied to the clearing electrode. This cloud profile is summed over the time corresponding to the passage of 34 bunches followed by 45 empty rf buckets. The transverse distribution is similar to

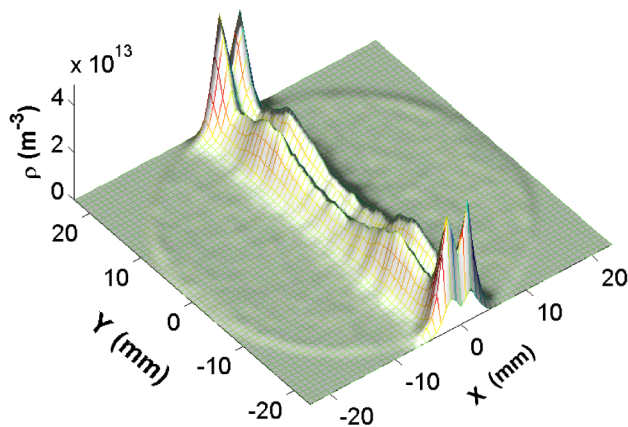


FIG. 15. Simulated EC distribution in transverse plane at the position of maximum vertical magnetic field component in the wiggler for the case of no clearing voltage.

that found in simulations of cloud buildup in a dipole magnet, since photoelectrons produced on the top and bottom of the vacuum chamber are trapped on the vertical field lines. The peak electron density averaged over the beam pipe which is present at arrival of the last bunch along the bunch train is about  $1.2 \times 10^{13} \text{ m}^{-3}$ . The photoelectrons generated at the vertical magnetic field null between poles can contribute a horizontal stripe with low density due to the lack of multiplication [31]. Such a density is negligible compared to that shown here. However, such electrons can persist on a time scale long compared to the revolution period due to mirroring [31].

The curved clearing electrode foreseen for the wiggler vacuum chambers has a width of 20 mm and is located on

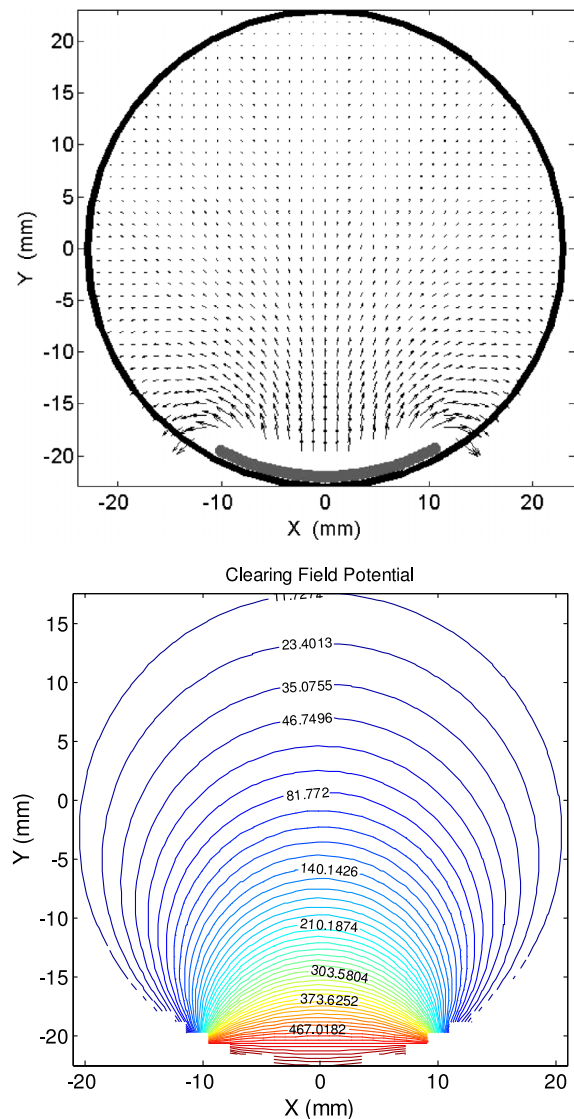


FIG. 16. The clearing electrode electric field in the simulated wiggler vacuum chamber for an electrode voltage of 500 V. The top plot shows the field vectors. The bottom plot shows equipotential lines labeled in units of volts.

the bottom of the chamber. The electrode design consists of a tungsten thermal spray on an alumina insulator. We have conservatively assumed the copper SEY parameters for the electrode surface as well. Figure 16 shows the field pattern for the simulated clearing electrode. The potential values on the equipotential lines allow an estimation of the clearing efficiency for cloud electrons of given kinetic energies. Since the electrons primarily impact the chamber surface near the vertical midplane, the clearing field near that region is important for the suppression of electron multiplication. Secondary electrons produced between bunch passages carry energies of just a few electron volts, so a weak clearing potential is sufficient to prevent them from approaching or leaving the electrode surface.

We simulated electrode voltages from  $-600$  V to  $+600$  V and found that a positive electrode bias of  $100$  V is sufficiently effective at suppressing multipacting. Figure 17 shows the effect of biases up to  $600$  V. With a positive clearing voltage, there are only a small number of macroparticles near the beam, so the modeled density

shows statistical fluctuations. The density near the positron beam is less than  $4 \times 10^{10} \text{ m}^{-3}$ , and the density averaged over the vacuum chamber is less than  $2 \times 10^{11} \text{ m}^{-3}$ .

A negative electrode bias also clears cloud electrons, but is less effective, as shown in Fig. 18, especially when the voltage is low. A strong field is required to clear the EC. Interestingly, the suppression is not a monotonic function of the clearing voltage. For instance, the average electron density for  $-300$  V is larger than that of  $-200$  V. The complicated dynamics due to the clearing field, positron beam kick, and space charge field accounts for this non-monotonic dependence.

The fundamental difference between positive and negative clearing voltages is the location where electron multipacting is suppressed. With a positive voltage, the photoelectrons and secondary electrons from the electrode surface are confined near the surface of the clearing electrode. After a low-energy secondary electron is emitted from the electrode, it follows the magnetic field lines upward and is turned back to the electrode by the clearing

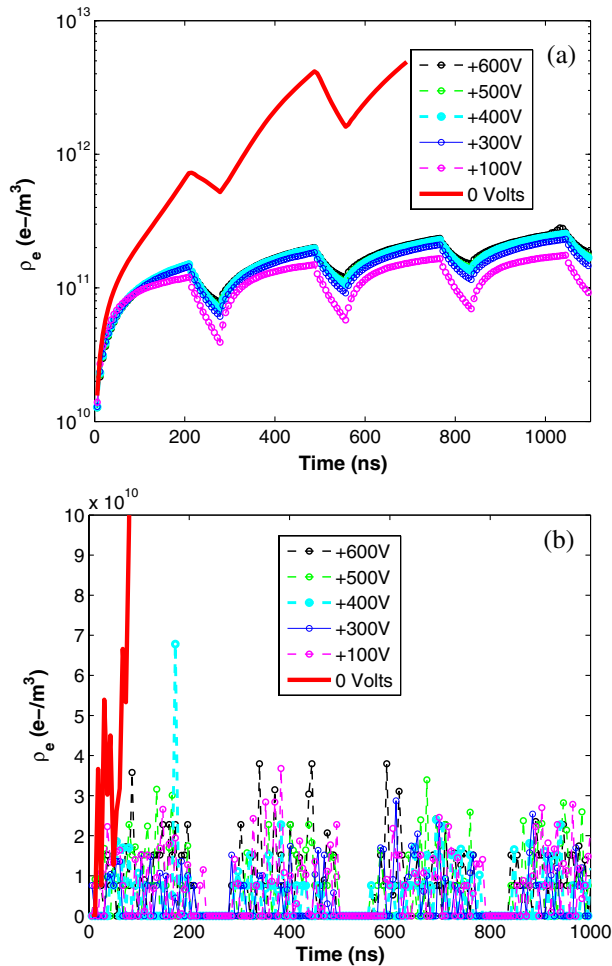


FIG. 17. Simulated buildup of the EC at the center of a wiggler pole with a positive clearing voltage applied: (a) cloud density averaged over the vacuum chamber, (b) central cloud density.

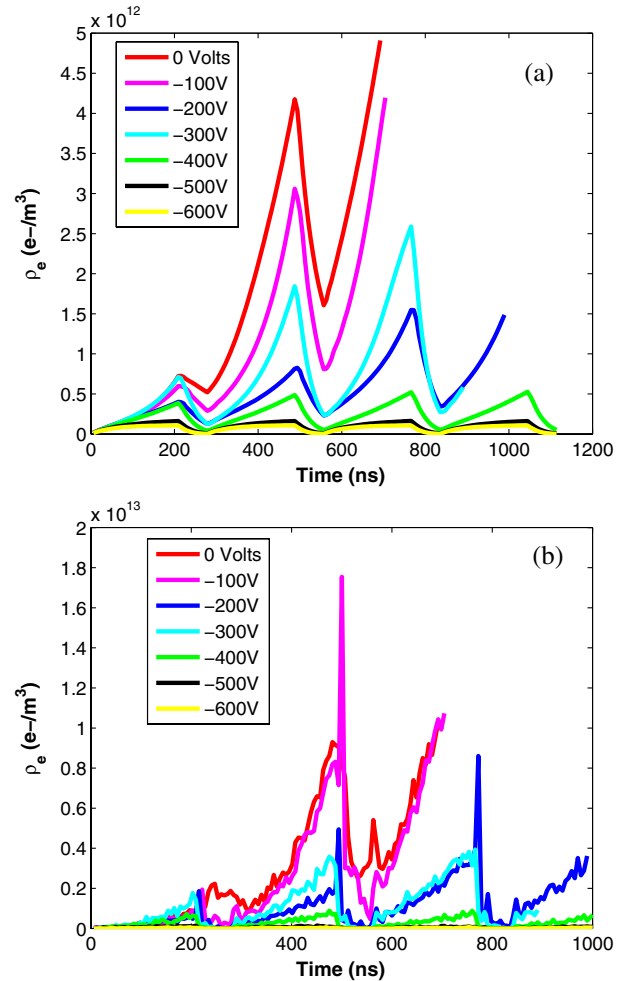


FIG. 18. Simulated buildup of the EC at the center of a wiggler pole with a negative clearing voltage applied: (a) cloud density averaged over the vacuum chamber, (b) central cloud density.

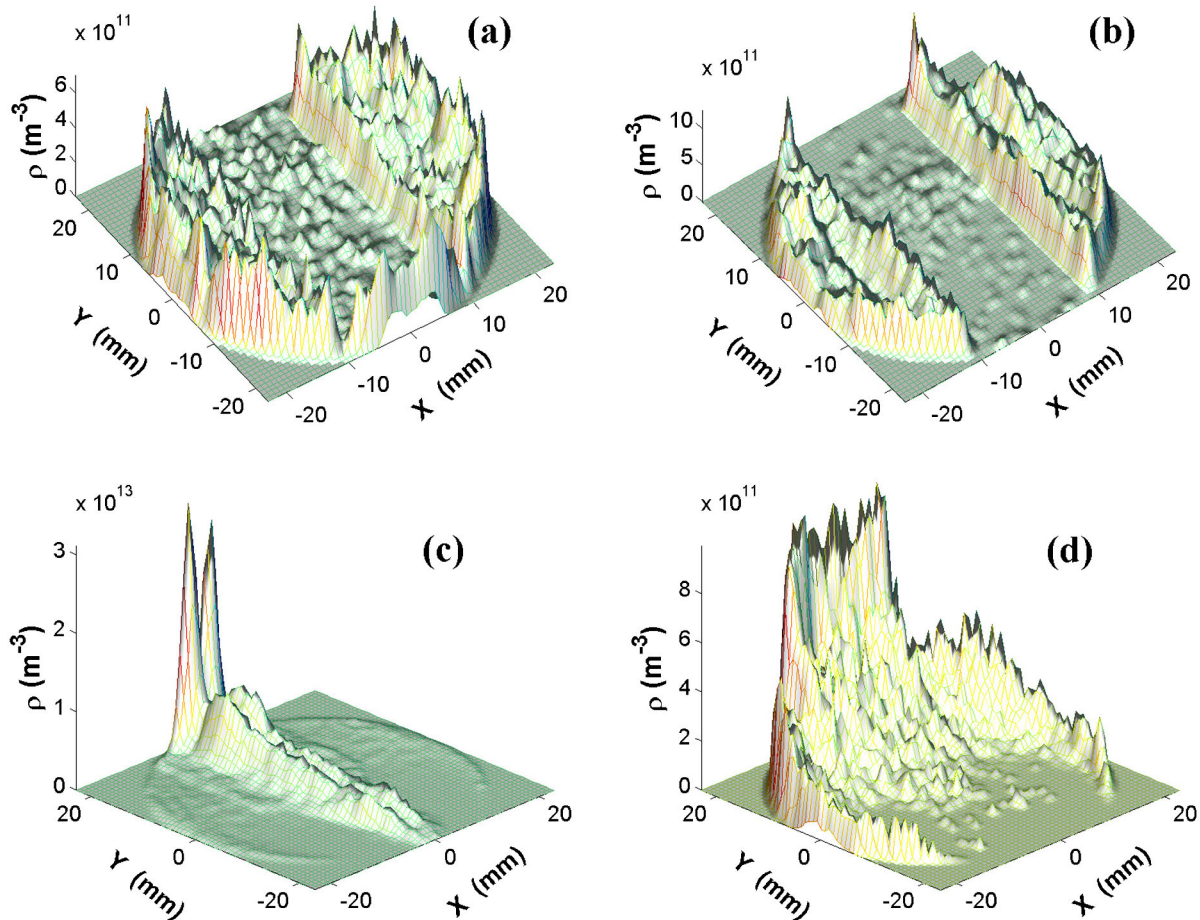


FIG. 19. Simulated EC transverse distributions at a wiggler magnet pole center for four values of the clearing voltage: (a) +100 V; (b) +600 V; (c) -300 V; (d) -600 V.

field. The secondary electrons are thus confined near the electrode surface. The electrons near the electrode surface can be clearly seen in Fig. 19(a) where a weak voltage of 100 V is applied. When the voltage is increased to +600 V, the electrons are closer to the electrode surface and disappear entirely in Fig. 19(b).

Figure 19(a) shows that a weak positive voltage results in a low-density region with the same horizontal width as the electrode. The suppression of the cloud is effective only over the horizontal region covered by the electrode. The photoelectrons and secondary electrons emitted from the top of the chamber spiral downward and reach the electrode surface. These electrons can have high enough kinetic energies to generate secondary electrons due to the acceleration imparted by the positron beam. However, secondary electrons thus produced will generally be trapped by the clearing field. Therefore, a positive bias effectively collects both the photoelectrons and secondary electrons.

In the case of a negative clearing voltage, both photoelectrons and secondary electrons can leave the electrode surface. The electrons emitted from the electrode surface are accelerated toward the beam axis and end up collecting near the top of the chamber, as can be seen in Figs. 19(c)

and 19(d). Although this results in clearing the cloud from the beam region, the clearing field near the top of the surface is much weaker than near the electrode, and the field lines deviate from the vertical direction as shown in Fig. 16. This makes negative biases much less effective for clearing the cloud, so a much stronger field is required. A voltage of -300 V does not suppress the multiplication. Even a voltage of -600 V does not significantly reduce the density of electrons near the center of the beam pipe and there remain a large number of electrons near the upper surface.

## VIII. BEAM DYNAMICS SIMULATION

Single-bunch instabilities and the dilution of vertical emittance is a primary concern of EC effects in DRs [32–34]. The modeling work on EC buildup described above provides estimates of the cloud density in the region near the beam at the arrival times of the bunches. The estimates place an upper limit on the ring-averaged density of about  $3.5 \times 10^{10} \text{ m}^{-3}$ . The additional cloud buildup suppression provided by the grooved surfaces recommended for the arc dipole regions has yet to be calculated for the ILC DR

lattice. Based on these results for upper limits on the cloud densities, the simulation code CMAD [35] has been used to estimate single-bunch instability thresholds and emittance dilution arising from the beam-cloud interaction. The parameters used in these simulations were based on the DTC03 lattice design. The study was performed with two models of the ring beta functions. The first used a continuous-focusing model. The second involved the full lattice of the DR. The continuous-focusing model is highly simplified but is far more efficient in performing computations. This model was used to scan through a set of cloud densities in order to estimate the range over which the behavior transitions from gradual and linear to a fast exponential growth in emittance. It should be noted that effects of damping and diffusion due to synchrotron radiation emission are not included in the calculations. The time scales of radiation damping and quantum excitation are both much less than the instability growth time.

The CMAD simulation algorithms are similar to those of other programs such as HEADTAIL [36], WARP [37], and PEHTS [38]. Results from CMAD, HEADTAIL, and WARP have been compared for the continuous-focusing and full lattice cases [39,40]. The continuous-focusing model uses a constant beta function value that is obtained from the betatron tunes and the circumference. The model has no dispersion, so there is no variation of the beam size around the simulated ring. The model uses a number of beam-cloud interaction points (IPs) around the ring sufficient to avoid artificial resonances arising from the discreteness of beam-cloud interaction.

The details of the physical and computational parameters are given in Tables V and VI, respectively. Our simulations assume chromaticity values typical of storage rings such as CESR. Collective effects require that the chromaticity be set to a reasonable value to ensure stability via chromatic damping. The computational parameters were chosen based on experience with simulations for CESRTA [41,42]. The computational domain was truncated at 20 rms beam sizes in the transverse directions and at 2 rms beam sizes in either direction for the longitudinal extent. The large transverse extent ensures that sufficient EC is included to accurately model the pinching process. The number of IPs used in the continuous-focusing model

TABLE V. List of physical parameters used in the CMAD simulations, corresponding to the ILC DR lattice design.

Beam energy	5 GeV
Unnormalized emittance $x, y$	0.5676 nm, 2.0 pm
Bunch population	$2 \times 10^{10}$
Bunch length	0.6036 cm
Tunes $x, y, z$	48.248, 26.63, 0.0314
Momentum compaction	$3.301 \times 10^{-3}$
Circumference	3234.3540 m
Energy spread	$1.1 \times 10^{-3}$
Chromaticity ( $\xi_x = \xi_y$ )	1.0

TABLE VI. List of computational parameters used in the CMAD simulations. The number of IPs is used only in the continuous-focusing model.

Macro e+	300000
Macro e-	100000
Bunch slices	96
Grid nodes	$128 \times 128$
Domain extent $x, y$	20 sigma
Domain extent $z$	$\pm 2$ sigma
IPs (uniform $\beta$ only)	400
Nr processors used in parallel	96

was 400, much greater than the number of betatron oscillations per revolution (see Table V). The beam was sliced longitudinally into 96 segments and the computation was performed in parallel, distributed over 96 processors.

Figure 20 shows the calculated emittance growth over a period of 500 turns using the continuous-focusing model. The simulations were done for EC densities ranging from  $1.0 \times 10^{10} \text{ m}^{-3}$  to  $5.0 \times 10^{11} \text{ m}^{-3}$ . Figure 20(a) shows the emittance growth rate for three cases, with the intermediate cloud density of  $3.5 \times 10^{10} \text{ m}^{-3}$  corresponding to the estimated ring-averaged cloud density in the vicinity of the beam. Increasing the cloud density to  $5.0 \times 10^{10} \text{ m}^{-3}$  results in no deviation from a linear dependence on turn number. Figure 20(b) shows that the vertical emittance growth rate increases by almost two orders of magnitude when the cloud density increases from  $3.5 \times 10^{10} \text{ m}^{-3}$  to  $3.0 \times 10^{11} \text{ m}^{-3}$ . Figure 20(c) shows that the growth rate transitions from linear to exponential when the density is raised to  $5.0 \times 10^{11} \text{ m}^{-3}$ . The linear region below the “instability threshold” has been observed in single-bunch simulations with other modeling codes [33,43]. The operating conditions of the ring must be kept well below the transition from linear to exponential dependence in order to ensure stable operation. Our results show that the cloud density for the ILC DR operating conditions can be expected to be an order of magnitude below this transition point.

Estimates of emittance growth were also calculated using the full lattice design of the DR. The beam particles were transported using first-order  $6 \times 6$  transfer matrices, thus including variation of the horizontal and vertical beam size with beta function and dispersion. In particular, the beam size ratio  $\sigma_x/\sigma_y$  reached a value of about 100, imposing challenging numerical accuracy conditions. This was overcome by altering the Poisson solver at points with a beam aspect ratio higher than 20. The beam underwent an interaction with the EC at each element in the lattice. Thus the number of IPs used in this case was 5765, equal to the number of elements in the lattice design model. The wigglers were modeled using a bend-drift-bend sequence. Electrons in regions with an applied magnetic field, including those in the wiggler sections, were tracked based

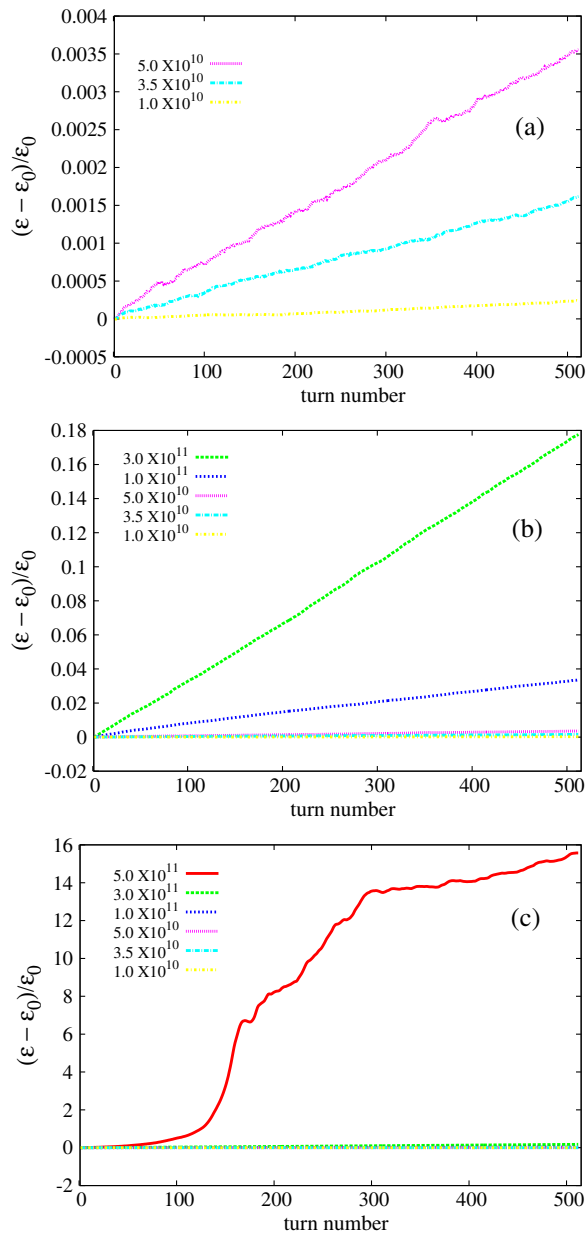


FIG. 20. Modeled relative vertical emittance growth using the continuous-focusing model for various cloud densities. (a) The relative growth rate over 500 turns is 0.16% for an average density of  $3.5 \times 10^{10} \text{ m}^{-3}$ , which is the value determined by the cloud buildup modeling for the ILC DR. (b) The growth rate increases to 18% in 500 turns for a density of  $3.0 \times 10^{11} \text{ m}^{-3}$ . (c) Exponential growth is found for a density of  $5.0 \times 10^{11} \text{ m}^{-3}$ .

on the full Lorentz force exerted on the particle. The influence of the external field influences the pinching process, a feature that is missing in the continuous-focusing calculations. The cloud density in each element was set to the value derived from the buildup simulations. These densities are listed in Table VII. Thus, several physical details omitted from the continuous-focusing model were taken into account in this simulation of the full lattice.

TABLE VII. Cloud density in the ring elements and their occupancy fractions.

Element	Cloud density	Occupancy (%)
Fieldfree	0	66
Dipoles	$4.0 \times 10^{10}$	15.14
Quads in arcs	$1.6 \times 10^{11}$	9.8
Sextupoles in arcs	$1.4 \times 10^{11}$	5.56
Wigglers	$1.5 \times 10^{10}$	2.96
Quads in wiggler region	$1.2 \times 10^{12}$	0.49
Average	$3.5 \times 10^{10}$	

Figure 21 shows the evolution of the beam emittance under the EC conditions given in Table VII. The calculation estimates the relative emittance growth over 300 turns to be 0.16%. Except for an initial transient phase in the first 25 turns, the growth is linear. The ILC DR beam store time is 18550 turns. In the absence of any damping mechanism over this time period, one can therefore expect the beam emittance to increase by 10% due to ECs during the store time. When the same extrapolation is applied to the continuous-focusing case with a cloud density of  $3.5 \times 10^{10} \text{ m}^{-3}$ , we obtain a growth of 6% in beam emittance during 18550 turns.

We have investigated the dependence of this result on the chosen chromaticity. Computations were performed using the continuous-focusing model with the cloud density of  $3.5 \times 10^{10} \text{ m}^{-3}$  given by the buildup simulations. For the purposes of this investigation of the chromaticity dependence, 40 beam-cloud interaction points were used, rather than the 400 modeled in the full simulation. Figure 22 shows that the chromaticity influences the emittance growth only moderately for this cloud density. The calculated emittance grows from 0.8% to 1.0% as the chromaticity increases from 0 to 6.

Future work on the beam dynamics simulation will include modeling of the detailed vacuum chamber cross

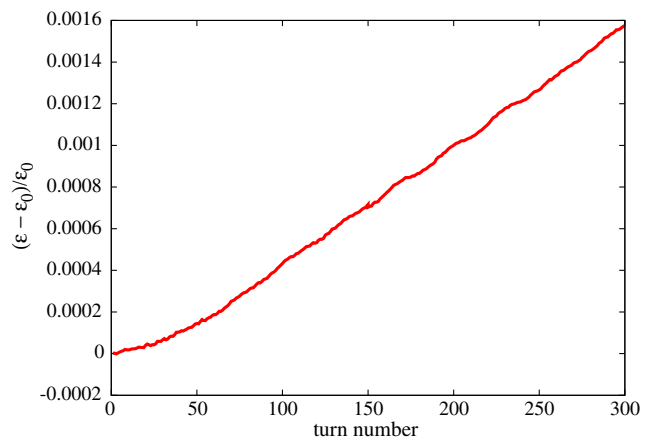


FIG. 21. Estimate of the emittance growth using the full lattice in the model with specified cloud densities in each element of the lattice.

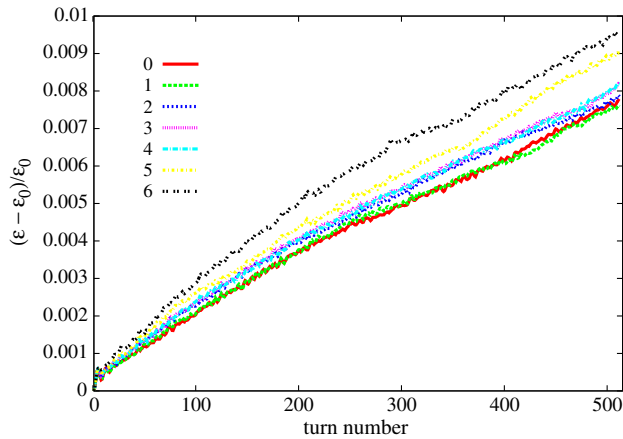


FIG. 22. Calculation of emittance growth for chromaticity values ranging from 0 to 6 in units of  $\xi = dQ/d\delta$  where  $\delta$  is the relative energy spread in the positron beam. These calculations were performed using the continuous-focusing model with a ring-averaged cloud density of  $3.5 \times 10^{10} \text{ m}^{-3}$ .

section. Rather than using a uniform distribution of cloud electrons, the initial electron cloud distribution for these simulations should be imported from the buildup calculations. In addition, the tracking of the beam should be performed for the full store period of the damping ring and include the damping and diffusion effects.

## IX. SUMMARY

We have updated the lattice design for the 3.2-km, 5 GeV ILC positron damping ring and calculated the distributions of synchrotron radiation around the ring, including the effects of photon scattering inside the vacuum chamber. This analysis was used to refine the choice of electron-cloud-mitigating techniques in the various magnetic field environments of the arcs and straights. Groove patterns and antechambers were used as mitigation techniques in the modeled dipole magnets, along with TiN-coating in the 5-cm-diameter quadrupole and sextupole magnet vacuum chambers. The drift regions were assumed to be equipped with solenoid windings and the wigglers with clearing electrodes. Electron buildup modeling codes tuned to the measurements of cloud buildup performed at the CESR Test Accelerator were employed to make quantitative estimates of the cloud densities near the beam axis at the arrival time of each of the 6-mm-long bunches for the operational bunch configuration of 34-bunch trains separated by 20 m, the bunches spaced 1.8 m apart, each carrying  $2 \times 10^{10}$  positrons. An upper limit on the ring-averaged electron density was found to be  $3.5 \times 10^{10} \text{ m}^{-3}$ . The cloud densities in the various ring sections then served as input to simulations of their effect on the positron beam emittance. The calculated emittance growth for these operating conditions was found to grow linearly with turn number, showing that operation was well below the

instability threshold. Total vertical emittance growth during the entire store time of 18550 turns was found to be about 10%. We can therefore positively assess the operational feasibility of the ILC positron damping ring as specified in the technical design report. This work will serve as a baseline for future optics development, vacuum chamber designs, and operating parameters of the ring.

## ACKNOWLEDGMENTS

The authors wish to acknowledge important contributions from the technical staffs of the collaborating laboratories. Our work also benefited from useful discussions with S. Calatroni, J. Calvey, R. Cimino, P. Costa Pinto, T. Demma, K. Kanazawa, S. Kato, Y. Li, K. Ohmi, G. Rumolo, Y. Suetsugu, M. Taborelli, M. Venturini, C. Yin Vallgren, and F. Zimmermann. This work is supported by the National Science Foundation and by the U.S. Department of Energy under Contract No. PHY-0734867, No. PHY-1002467, No. DE-FC02-08ER41538, and No. DE-SC0006505. This beam dynamics simulations also used resources of the National Energy Research Scientific Computing Center, which is supported by the Office of Science of the U.S. Department of Energy under Contract No. DE-AC02-05CH11231.

- [1] G. Aad *et al.* (ATLAS Collaboration), *Phys. Lett. B* **716**, 1 (2012).
- [2] S. Chatrchyan *et al.* (CMS Collaboration), *Phys. Lett. B* **716**, 30 (2012).
- [3] T. Behnke, J.E. Brau, B. Foster, J. Fuster, M. Harrison *et al.*, [arXiv:1306.6327](https://arxiv.org/abs/1306.6327).
- [4] K. Ohmi, *Phys. Rev. Lett.* **75**, 1526 (1995).
- [5] M. A. Furman and G. R. Lambertson, in *Proceedings of MBI97: International Workshop on Multibunch Instabilities in Future Electron and Positron Accelerators, Tsukuba, Japan, 1997*, edited by Y.H. Chin (KEK, Tsukuba, Japan, 1997), p. 170.
- [6] J. Shanks and D. Rubin, in *2012 International Workshop on Future Linear Colliders, Arlington, TX* (2012).
- [7] M. Korostelev and A. Wolski, in *Proceedings of the International Particle Accelerator Conference, Kyoto, Japan* (ICR, Kyoto, 2010), p. 3575.
- [8] C. Adolphsen, M. Barone, B. Barish, K. Buesser, P. Burrows *et al.*, [arXiv:1306.6328](https://arxiv.org/abs/1306.6328).
- [9] J. A. Crittenden, M. A. Palmer, and D.L. Rubin, in *Proceedings of the 3rd International Particle Accelerator Conference, New Orleans, LA, 2012* (IEEE, Piscataway, NJ, 2012), p. 1969.
- [10] J. Shanks, D. L. Rubin, J. A. Crittenden, and M. Palmer, in *Proceedings of the 3rd International Particle Accelerator Conference, New Orleans, LA, 2012* (IEEE, Piscataway, NJ, 2012), p. 1972.
- [11] M. T. F. Pivi, L. Wang, T. Demma, S. Guiducci, Y. Suetsugu, K. Shibata, K. Ohmi, G. F. Dugan, M. Palmer, J. A. Crittenden, K. Harkay, L. Boon, M. A. Furman, and C. Yin Vallgren, in *Proceedings of the 2nd International*

- Particle Accelerator Conference, San Sebastián, Spain* (EPS-AG, Spain, 2011), p. 1063.
- [12] J. Conway, Y. Li, and M. Palmer, in *Proceedings of the 3rd International Particle Accelerator Conference, New Orleans, LA, 2012* (IEEE, Piscataway, NJ, 2012), p. 1960.
- [13] G. F. Dugan and D. Sagan, in *Proceedings of ELOUD 2010: 49th ICFA Advanced Beam Dynamics Workshop on Electron Cloud Physics, Ithaca, NY*, edited by K. Smolenski (2013), p. 118.
- [14] O. B. Malyshev, J. M. Lucas, N. Collomb, S. Postlethwaite, M. Korostelev, A. Wolski, and K. Zolotarev, in *Proceedings of the International Particle Accelerator Conference, Kyoto, Japan* (ICR, Kyoto, 2010), p. 3563.
- [15] K. Zolotarev, N. Collomb, M. Korostelev, J. Lucas, S. Postlethwaite, A. Wolski, and O. Malyshev, in *Proceedings of the International Particle Accelerator Conference, Kyoto, Japan* (ICR, Kyoto, 2010), p. 3569.
- [16] L. Boon, A. Garfinkel, and K. Harkay, in *Proceedings of the 2nd International Particle Accelerator Conference, San Sebastián, Spain* (EPS-AG, Spain, 2011), p. 3332.
- [17] M. A. Furman and M. T. F. Pivi, *Phys. Rev. ST Accel. Beams* **5**, 124404 (2002).
- [18] M. A. Furman, in *Proceedings of ELOUD 2010: 49th ICFA Advanced Beam Dynamics Workshop on Electron Cloud Physics, Ithaca, NY*, edited by K. Smolenski (2013), p. 194.
- [19] G. F. Dugan, M. A. Palmer, and D. L. Rubin, in *ICFA Beam Dynamics Newsletter*, No. 50, edited by J. Urakawa (International Committee on Future Accelerators, 2009), p. 11.
- [20] J. Kim, D. Asner, J. Conway, S. Greenwald, Y. Li, V. Medjidzade, T. Moore, M. Palmer, and C. Strohman, in *Proceedings of the 24th Particle Accelerator Conference, PAC-2011, New York, NY* (IEEE, New York, 2011), p. 1253.
- [21] L. Wang, K. Bane, C. Chen, T. Himel, M. Munro, M. Pivi, T. Raubenheimer, and G. Stupakov, in *Proceedings of the 22nd Particle Accelerator Conference, PAC-2007, Albuquerque, NM*, edited by C. Petit-Jean-Genaz (IEEE, New York, 2007), p. 4234.
- [22] M. Venturini, M. Furman, J.-L. Vay, and M. Pivi, in *Proceedings of the 22nd Particle Accelerator Conference, PAC-2007, Albuquerque, NM*, edited by C. Petit-Jean-Genaz (IEEE, New York, 2007), p. 2993.
- [23] M. T. F. Pivi, F. K. King, R. E. Kirby, T. Markiewicz, T. O. Raubenheimer, J. Seeman, and L. Wang, in *Proceedings of the 11th European Particle Accelerator Conference, Genoa, 2008* (EPS-AG, Genoa, Italy, 2008), p. 691.
- [24] M. Pivi, F. K. King, R. E. Kirby, T. O. Raubenheimer, G. Stupakov, and F. Le Pimpec, *J. Appl. Phys.* **104**, 104904 (2008).
- [25] J. A. Crittenden, Y. Li, X. Liu, M. A. Palmer, and J. P. Sikora, in *Proceedings of the 4th International Particle Accelerator Conference, IPAC2013, Shanghai, China* (JACoW, Shanghai, China, 2013), p. 846.
- [26] G. Rumolo and F. Zimmermann, CERN Technical Report No. CERN-SL-Note-2002-016-AP, CERN, Geneva, Switzerland, 2002.
- [27] G. Rumolo, F. Ruggiero, and F. Zimmermann, *Phys. Rev. ST Accel. Beams* **4**, 012801 (2001); **4**, 029901(E) (2001).
- [28] J. A. Crittenden and J. P. Sikora, in *Proceedings of ELOUD 2012: Joint INFN-CERN-EuCARD-AccNet Workshop on Electron-Cloud Effects, La Biodola, Elba, Italy*, Report No. CERN-2013-002, edited by R. Cimino, G. Rumolo, and F. Zimmermann (CERN, Geneva, 2013), p. 241.
- [29] J. R. Calvey, J. A. Crittenden, G. Dugan, M. A. Palmer, and C. M. Celata, in *Proceedings of the 23rd Particle Accelerator Conference, Vancouver, Canada, 2009* (IEEE, Piscataway, NJ, 2009), p. 3306.
- [30] J. A. Crittenden, J. R. Calvey, G. F. Dugan, D. L. Kreinick, Z. Leong, J. A. Livezey, M. A. Palmer, D. L. Rubin, D. C. Sagan, K. Harkay, R. L. Holtzapple, M. A. Furman, G. Penn, M. Venturini, M. Pivi, and L. Wang, in *Proceedings of the International Particle Accelerator Conference, Kyoto, Japan* (ICR, Kyoto, 2010), p. 1976.
- [31] L. Wang, X. Huang, and M. Pivi, in *Proceedings of the International Particle Accelerator Conference, Kyoto, Japan* (ICR, Kyoto, 2010), p. 1892.
- [32] G. F. Dugan, M. Billing, K. Butler, J. A. Crittenden, M. Forster, D. Kreinick, R. Meller, M. Palmer, G. Ramirez, M. Rendina, N. Rider, K. Sonnad, H. Williams, J. Chu, R. Campbell, R. Holtzapple, M. Randazzo, J. Flanagan, K. Ohmi, M. Furman, M. Venturini, and M. Pivi, in *Proceedings of the 3rd International Particle Accelerator Conference, New Orleans, LA, 2012* (IEEE, Piscataway, NJ, 2012), p. 2081.
- [33] H. Jin, M. Yoon, K. Ohmi, J. W. Flanagan, and M. A. Palmer, *Jpn. J. Appl. Phys.* **50**, 026401 (2011).
- [34] F. Zimmermann, *Phys. Rev. ST Accel. Beams* **7**, 124801 (2004).
- [35] M. T. F. Pivi, in *Proceedings of the 22nd Particle Accelerator Conference, PAC-2007, Albuquerque, NM*, edited by C. Petit-Jean-Genaz (IEEE, New York, 2007), p. 3636.
- [36] G. Rumolo and F. Zimmermann, *Phys. Rev. ST Accel. Beams* **5**, 121002 (2002).
- [37] J.-L. Vay, A. Friedman, and D. P. Grote, in *Proceedings of ICAP 2006: International Computational Accelerator Physics, Chamonix, France* (2006), p. 2562.
- [38] K. Ohmi, in *Proceedings of the Particle Accelerator Conference, Chicago, IL, 2001*, edited by P. Lucas and S. Webber (IEEE, New York, 2001), p. 1895.
- [39] J.-L. Vay, C. M. Celata, M. A. Furman, G. Penn, M. Venturini, D. P. Grote, and K. G. Sonnad, in *Proceedings of the 23rd Particle Accelerator Conference, Vancouver, Canada, 2009* (IEEE, Piscataway, NJ, 2009), p. 4719.
- [40] K. G. Sonnad, M. T. F. Pivi, J.-L. Vay, G. Rumolo, R. Tomas, F. Zimmermann, and G. Franchetti, in *Proceedings of ELOUD 2010: 49th ICFA Advanced Beam Dynamics Workshop on Electron Cloud Physics, Ithaca, NY*, edited by K. Smolenski (2013), p. 100.
- [41] K. G. Sonnad, K. Butler, G. Dugan, M. A. Palmer, and M. T. F. Pivi, in *Proceedings of the 24th Particle Accelerator Conference, PAC-2011, New York, 2011* (IEEE, New York, 2011), p. 1683.
- [42] J. W. Flanagan, H. Fukuma, H. Ikeda, T. Mitsuhashi, G. S. Varner, J. P. Alexander, N. Eggert, W. H. Hopkins, B. Kreis, M. A. Palmer, and D. P. Peterson, in *Proceedings of the 2010 International Particle Accelerator Conference, Kyoto, Japan* (ICR, Kyoto, 2010), p. 966.
- [43] E. Benedetto, G. Franchetti, and F. Zimmermann, *Phys. Rev. Lett.* **97**, 034801 (2006).